A minimalist and robust chemo-photothermal nanoplatform capable of augmenting autophagy-modulated immune response against breast cancer

Hui Ming [a,1], Bowen Li [a,1], Hailong Tian [a,1], Li Zhou [a], Jingwen Jiang [a], Tingting Zhang [a], Ling Qiao [b], Peijie Wu [b], Edouard C. Nice [c], Wei Zhang [d,e], Weifeng He [f,***], Canhua Huang [a,*], Haiyuan Zhang [g,**]

[a] State Key Laboratory of Biotherapy and Cancer Center, West China Hospital and West China School of Basic Medical Sciences and Forensic Medicine, Sichuan University and Collaborative Innovation Center for Biotherapy, Chengdu, 610041, PR China
[b] School of Basic Medical Sciences, Chengdu University of Traditional Chinese Medicine, Chengdu, China
[c] Department of Biochemistry and Molecular Biology, Monash University, Clayton, VIC, 3800, Australia
[d] West China Biomedical Big Data Center, West China Hospital, Sichuan University, Chengdu, 610041, China
[e] Mental Health Center and Psychiatric Laboratory, The State Key Laboratory of Biotherapy, West China Hospital of Sichuan University, Chengdu, China
[f] Institute of Burn Research, Southwest Hospital, State Key Laboratory of Trauma, Burn and Combined Injury, Chongqing Key Laboratory for Disease Proteomics, Army Military Medical University, Chongqing, 400038, China
[g] School of Basic Medicine, Health Science Center, Yangtze University, Jingzhou, China

ARTICLE INFO

ABSTRACT

Previously used in anti-fungal therapy, itraconazole has now been shown to be successful in treating advanced breast cancer (NCT00798135). However, its poor solubility still restricts its application in clinical treatment. There is therefore an urgent need for combined methods to enhance the therapeutic effect of itraconazole (IC) in breast cancer treatment. With this goal, co-assembled IC/IR820 NPs with synergistic photonic hyperthermia and itraconazole payloads have been constructed to overcome these shortcomings. The IC/IR820 NPs show an enhanced therapeutic effect on breast cancer by inducing reactive oxygen species (ROS)-mediated apoptosis and autophagic death. Further evaluation in a mouse model has shown impressive effects of the IC/IR820 NPs on both inhibiting tumor metastasis and activating immunity to prevent tumor recurrence. Mechanistically, itraconazole may promote both tumor cell antigen presentation through autophagy and the activation of dendritic cells to induce an immune response, which displays a synergistic effect with the immune response generated by photo-thermal therapy to inhibit tumor recurrence. This strategy of combining itraconazole and IR820 into one mini-malist and robust nanoplatform through co-assembly results in excellent therapeutic efficacy, suggesting its potential application as an alternative method for the clinical treatment of breast cancer.

1. Introduction

To date, breast cancer remains one of the most lethal tumors worldwide [1]. Despite many advances in breast cancer research, breast cancer still accounts for ~15% of all cancer deaths in the United States. The 5-year survival rate of distant breast cancer is only 29% compared to 86% for regional breast tumors, mainly due to metastasis and recurrence [2]. Although various breast cancer treatments have been developed, the therapeutic effect on advanced breast cancer is still not adequate [3].

New therapeutic modalities therefore urgently need to be developed to improve breast cancer treatment outcomes.

Itraconazole was initially used to treat fungal infections, but recent studies have shown that it has excellent effects in advanced cancer treatment [4–7]. Itraconazole exerts this anti-tumor effect in various ways, including promoting reactive oxygen species (ROS)-mediated apoptosis and autophagic cell death, inhibition of the Hedgehog pathway, and preventing metastasis [8–10]. Itraconazole can disrupt mitochondrial membrane potential and promote a massive accumulation

of ROS, leading to apoptotic and autophagic cell death in various tumors, including breast, liver, prostate, lung, and basal cell cancers [10–12]. In addition, itraconazole may inhibit epithelial-mesenchymal transition (EMT) by modulating the activation of the Hedgehog pathway [13,14]. Furthermore, itraconazole-induced autophagy can promote antigen presentation to dendritic cells, leading to activation of the immune response against the tumor [15,16]. Recent studies have demonstrated that itraconazole has an excellent performance in inhibiting both tumor metastasis and recurrence [5,17], and it is currently under clinical evaluation for patients with advanced tumors, including metastatic breast cancer (NCT00798135). However, the poor solubility of itraconazole (1–4 ng/mL in water) limits the scope of its clinical application [18].

Compared with chemotherapy and targeted therapy, photothermal therapy (PTT) has many unique advantages, including non-invasiveness, convenience, and fewer side effects, and is gaining increasing attention in breast cancer treatment [19,20]. PTT excites photothermal agents to generate heat through near-infrared (NIR) light irradiation, causing adjacent tumor cells to rupture through short-term heating, which leads to immunogenic cell death [21]. The NIR inflorescent dye new

Indocyanine Green (IR820) has been approved by the Food and Drug Administration (FDA) for clinical treatment due to its high photothermal conversion rate and low toxicity [22,23]. However, its clinical application has been limited due to poor targeting, short retention time, and insufficient efficacy in eliminating tumor cells [24]. Therefore, the use of IR820 in cancer therapy is usually combined with other treatments (e.g., chemotherapy, immunotherapy) [25,26].

Herein, we have designed a minimalist and robust chemo-photothermal nanoplatform capable of augmenting autophagy-modulated immune response against breast cancer metastasis and recurrence by co-assembling itraconazole and IR820 (IC/IR820 NPs, Scheme 1). This nanoplatform improves the poor-solubility of itraconazole and at the same time, enhances targeting and retention time through enhanced permeability and retention (EPR) effect owing to the particle diameter. In this case, IC/IR820 NPs promote cell apoptosis and autophagic cell death by activating ROS and inhibiting breast cancer tumor metastasis. In addition, IC/IR820 NPs can stimulate the maturation of dendritic cells by inducing autophagy, which synergizes with IR820-mediated immunogenic cell death in breast cancer. Moreover, IC/IR820 NPs inhibit the growth of distant tumors and tumor recurrence,
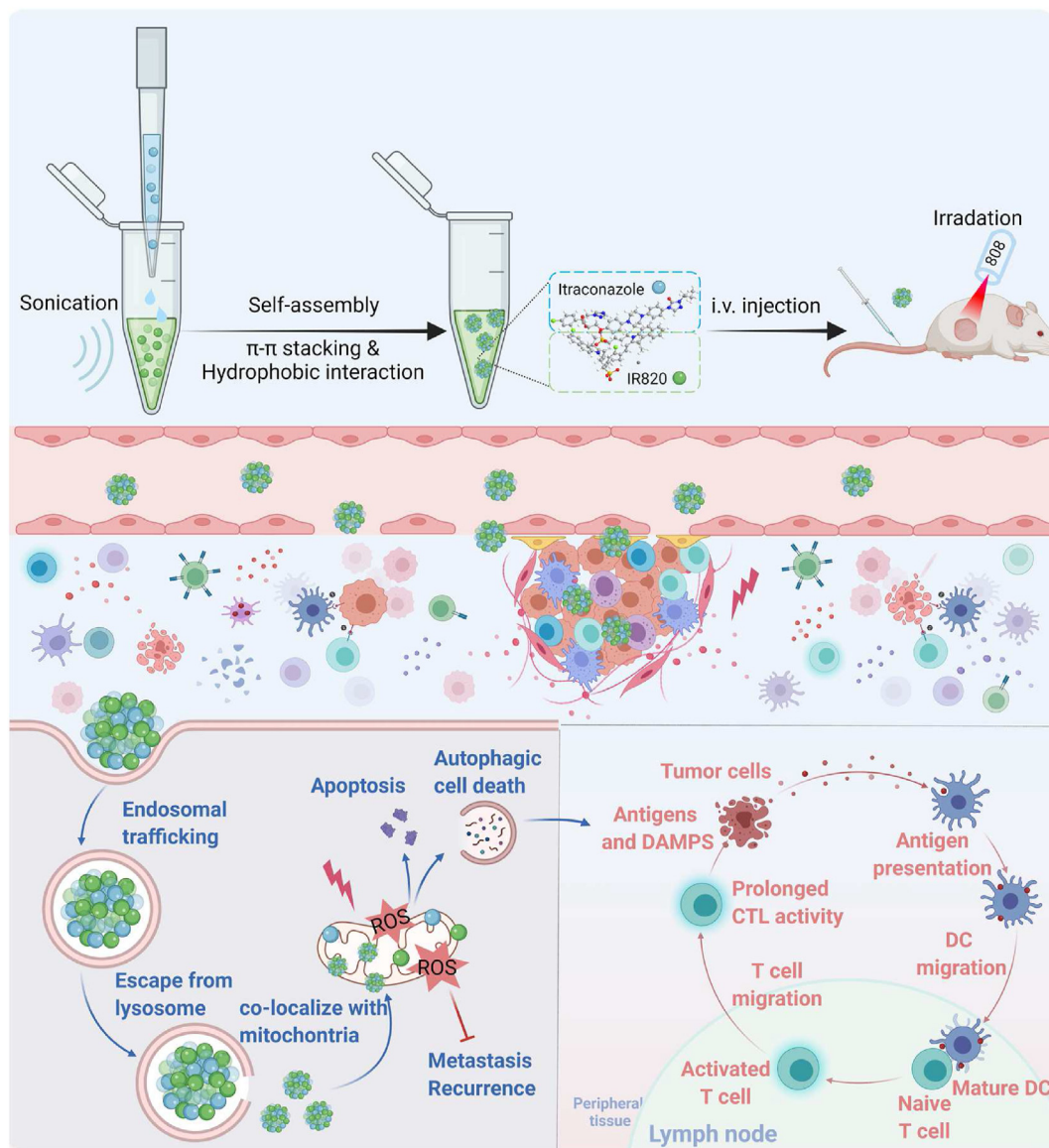
Scheme 1. The preparation of the IC/IR820 NPs allows amplified apoptosis, autophagy, and immunogenic cell death during breast cancer therapy. Created with BioRender.com.

which is expected to reduce minimal residual disease during breast cancer treatment. Therefore, our nanoplatform complements defects from each modality and enhances the advantages of both, with promising outcomes for clinical breast cancer treatment.

2. Materials and methods

2.1. Materials

Itraconazole (I129771) was purchased from Aladdin. IR820 (448014) was obtained from J&K Scientific. 3-methyladenine (3-MA) was purchased from MedChem Express. 3-(4,5-dimethylthiazol-2-yl)-2,5-diphenyltetrazolium bromide (MTT), dimethyl sulfoxide, crystal violet (C0775), and chloroquine (CQ) diphosphate salt (C6628) were purchased from Millipore Sigma. DAPI was purchased from Invitrogen. Sodium chloride injection was purchased from Sichuan Kelun Pharmaceutical Co., Ltd. Mel (Purity, 99.5%). Penicillin-streptomycin solution was manufactured for HyClone Laboratories. Fetal bovine serum albumin (FBS) was purchased from Biowest. Dulbecco's modified eagle medium (DMEM) was purchased from Thermo Fisher Biochemical Products (Beijing) Co., Ltd. The antibodies used were as follows: anti-β-actin was purchased from Santa Cruz Biotechnology; cleaved-caspase 3 caspase 3, p62, PARP, cleaved-PARP were acquired from Cell Signaling Technology; Ki67 was purchased from Bioss; and LC3 was purchased from Novus. Horseradish peroxidase-conjugated anti-rabbit secondary antibody was obtained from Santa Cruz Biotechnology. For immunofluorescence, goat anti-rabbit Alexa Fluor 488 and goat anti-mouse Alexa Fluor 594 were obtained from Thermo Fisher Scientific.

2.2. The preparation of IC/IR820 NPs

Briefly, itraconazole dichloromethane solution (2 mg/mL, 1 mL) and IR820 methanol solution (2 mg/mL, 1 mL) were mixed followed by ultrasonication for 5 min (PL-S40, Kangshijie, 240 W). After removing the solvent by rotary evaporation, the mixture was dispersed into 5 mL deionized water with sonication (5 min).

2.3. The characteristics of IC/IR820 NPs

The morphology of IC/IR820 NPs was observed by transmission electron microscopy (TEM, HT7800, Electron Microscope Room, West China School of Basic Medical Sciences & Forensic Medicine, Sichuan University). A zeta sizer nano analyzer (Malvern) was used to characterize the size distribution and zeta potential of IC/IR820 NPs.

2.4. In vitro photothermal performance

To determine the photothermal performance of the IC/IR820 NPs, 1 mL of IC/IR820 NPs solution was irradiated by 808 nm laser (1.0 W/cm^2). The temperature was detected by a digital thermometer at designated times. The photothermal conversion efficiency (η) was determined according to the following formula.

$$\eta(\%) = \frac{hS\Delta T_{max} - Q_{Dis}}{I\left(1 - 10^{-A_\lambda}\right)} \times 100\%$$

where h refers to the heat transfer coefficient, S refers to the surface area of the receptacle, ΔT_{max} refers to the temperature difference of the maximum system temperature and environmental temperature, Q_{Dis} refers to the heat dissipated from the laser mediated by the solvent, I refers to the laser power, and A_λ refers to the absorbance at a specific wavelength.

2.5. Cell culture

Human breast cancer cell lines MDA-MB-231, MCF-7, and mouse breast cancer cell line 4T1 were purchased from the American Type Culture Collection (Manassas, VA, USA). MCF-7 and 4T1 were maintained in DMEM, while MDA-MB-231 was maintained in RPMI 1640, supplemented with 10% FBS, 100 U/mL penicillin, and 100 U/mL streptomycin in a humidified incubator at 37 °C under 5% CO_2 atmosphere.

2.6. Detection of cell growth

The MTT assay was used to detect short-term effects of indicated reagents on tumor cell growth, using the procedure previously described by Jiang et al. [27]. Briefly, cells were seeded in 96-well plates (4000 cells/well) and treated for 24 h with the indicated concentrations of indicated reagents. The absorbance was measured at 490nm test wavelength and 570nm reference wavelength with an ELISA multi-well spectrophotometer.

The long-term effects on tumor cell proliferation were analyzed using a colony formation assay as described previously [28]. Cells were seeded in 24-well plates (500 cells/well) and treated with the indicated concentration of reagents. The medium was changed every 3 days. After 2 weeks, the colonies were stained with crystal violet for 30 min and washed 3 times.

2.7. Immunoblotting

Cells were washed with ice-cold PBS and then lysed with RIPA buffer (50 mM Tris, 1.0 mM EDTA, 150 mM NaCl, 0.1% SDS, 1% Triton X-100, 1% sodium deoxycholate, 1 mM PMSF). The samples were analyzed by immunoblotting with the indicated antibodies.

2.8. Immunofluorescence

Cells were plated on glass coverslips in 24-well plates (1.5×10^4 cells/well) for 24 h and fixed in 4% paraformaldehyde. After being washed with PBS, cells were permeabilized with 0.4% Triton X-100 followed by blocking with 5% fetal bovine serum. The indicated first antibodies and Alexa Fluor secondary antibodies were used for cells incubation. Images were viewed with a confocal laser scanning microscopy (Carl Zeiss, Oberkochen, Germany).

2.9. Immunohistochemistry

Tumor xenografts were formalin-fixed, paraffin-embedded, and sectioned in pre-adherent slides. Slides were subjected to the indicated first antibodies overnight. According to the protocol, the sections were incubated with secondary antibodies and then developed with 3,3′diaminobenzidine chromogen. All samples were visualized, and images were captured using a DM2500 fluorescence microscope (Danaher, Wetzlar, Germany). Quantitative scoring analyses were performed by multiplying the percentage of staining-positive cells area (A) by the intensity (B: 0, negative; 1, weakly positive; 2, positive; 3, strongly positive). The final score for each slide was calculated as A × B.

2.10. In vivo biodistribution of IC/IR820 NPs

4T1 cells (5×10^5) were injected into the mammary fat pad of female Balb/c mice. When the tumor reached 150–200 mm^3, free IR820 or IC/IR820 NPs were administered by tail vein injection (100 μL, free IR820, and IC/IR820 concentration 2 mg/kg). At 1, 2, 4, 6, 8, and 24 h after administration, mice were anesthetized and imaged using an IVIS Lumina III (CLS136334, PerkinElmer). The mice were sacrificed 24 h post-administration, and the tumors and major organs were harvested and subjected to *ex vivo* fluorescence imaging as mentioned above. The fluorescence from each organ was analyzed by the instrument software.

2.11. In vivo therapeutic effect of IC/IR820 NPs

Orthotopic 4T1 tumors were established as above, and treatment commenced when the average tumor volume reached about 100 mm^3. A total of 20 female Balb/c mice (8 weeks old) were randomly assigned to 4 groups (n = 5) and injected with sodium chloride injection, free IC, free IR820, or IC/IR820 NPs via the tail vein (2 mg/kg IC, 2 mg/kg IR820) every two days. All mice in the IR820 and IC/IR820 NPs-treated groups received 5 min laser irradiation 6h after tail vein injection (laser was placed ~1 cm above the tumor). The bodyweight of the mice was recorded daily. All the mice were sacrificed on day 17, and the tumors were collected, weighed, and taken for H&E and immunohistochemistry.

Tumor growth was monitored by digital calipers, and the volumes were calculated as following formula:

$$Tumor\ volume\ (mm^3) = \frac{length \times width^2}{2}$$

2.12. Bilateral anti-tumor effects and immunotherapy of distant tumor

4T1 cells (8×10^5) were subcutaneously inoculated into the left (the primary tumor) and right (distant tumor) flank regions of female Balb/c mice, respectively. The mice were separated into four groups NS, IC, IR820, or IC/IR820 NPs, randomly after the tumor volumes were about 100 mm^3. Then, the tumors were exposed to 808 nm laser (1 W/cm^2, 5 min). The tumor volumes and body weights were measured every day. After 10 days of indicated treatments, mice were sacrificed to analyze the CD4$^+$ T cells and CD8$^+$ T cells in distant tumors via flow cytometry.

2.13. Inhibition of postsurgical recurrence of 4T1 tumor

4T1 cells (1×10^6) were subcutaneously inoculated into the left flank region of female Balb/c mice. After the tumor volumes were about 500 mm^3, the tumors were removed by surgery, and the mice were randomly separated into four groups. NS, IC, IR820, or IC/IR820 NPs were intravenously injected at equivalent dosage. After 4 h, the tumors were exposed to 808 nm laser (1 W/cm^2, 5 min). The tumor volumes and body weights were measured daily.

2.14. Statistical analysis

All statistical analysis and graphics were performed using GraphPad 9 software (GraphPad, La Jolla, CA, USA). A one-way ANOVA or Student's t-test was used to analyze statistical differences. All data are presented as the mean with SD from at least three individual experiments. A value of $P < 0.05$ was considered statistically significant.

3. Results and discussion

3.1. Preparation and characterization of IC/IR820 NPs

Although itraconazole has shown promising therapeutic effects in pre-clinical research [6,17,29], the poor water solubility and low bioavailability have limited its clinical application (Fig. S1A). Recent studies suggest that engineered nanoparticles can transform the physicochemical properties of traditional drugs with poor solubility while achieving the synergistic effect of combined therapy [30]. Since PTT has been shown to have complementary advantages with chemotherapy drugs, we designed IC/IR820 NPs using the thin-film dispersion method to enhance breast cancer therapeutic efficacy. IC and IR820 (1:1 mass ratio rather than 1:2 or 2:1, Fig. S1B) can co-assemble into nanoparticles in aqueous solution due to their π-π and hydrophobic interactions based on the molecular structure [31].

The UV–vis absorbance spectra of IC/IR820 NPs were conducted to confirm the successful synthesis (Fig. 1A). The transmission electron

microscopy (TEM) image (Fig. 1B) demonstrated that the assembly had a well-defined spherical nanostructure. Furthermore, dynamic light scattering (DLS) results showed that the mean diameter of IC/IR820 nanoparticles was ~120.9 nm (Fig. 1C), which was suitable for passive tumor targeting due to the EPR effect [32–34]. Notably, IC/IR820 NPs remain stable in their size as measured by DLS after several days (Fig. S1C). The Tyndall effect was still clearly visible even ten days later (Fig. S1D), indicating the excellent stability of IC/IR820 NPs. The zeta potential of IC/IR820 NPs was ~-42.2 mV with good stability (Fig. S1E-F), which guaranteed a prolonged blood circulation time.

Next, the photothermal capacity of IC/IR820 NPs was investigated by measuring the temperature change during laser irradiation (808 nm, 1W/cm^2) in vitro (Fig. 1D–E, S1G). The increased temperature of both IC/IR820 NPs and free IR820 were concentration dependent. Interestingly, the increased temperature of IC/IR820 NPs was higher than free IR820 at different time points. The photothermal conversion efficiency (η) of IC/IR820 NPs was 29.2% with good photothermal stability (Fig. S1H-J). Therefore, IC/IR820 NPs could be used as an efficient nanoplatform for PTT.

### 3.2. Intracellular uptake and anti-breast cancer effect of IC/IR820 NPs

Nanoparticle uptake by cells is critical for efficient drug delivery to the cytoplasm or target organelles, as well as anti-tumor effect. Herein, we chose three breast cancer cell lines (MDA-MB-231, MCF-7, 4T1) to evaluate the cell uptake efficacy. Fluorescent images and cytometry results indicated that IC/IR820 NPs accumulated over time and reached satisfactory intracellular levels after 4 h (Fig. 1F–G, S2A-D). Free IR820 is taken in cells by passive diffusion, while IC/IR820 NPs are efficiently transported due to the favorite size and endocytosis. The fluorescent intensity of IC/IR820 NPs was higher than that of free IR820, which was consistent with the flow cytometry results (Fig. 1H–I, S2E-H). Taken together, these results demonstrated that the IC/IR820 NPs had the potential to serve as an ideal nanoplatform for effective co-deliver of IC and IR820 into cancer cells, enabling an effective chemo-phototherapeutic effect.

Next, we evaluated the cell viability of breast cancer cells using a 3-(4,5-dimethylthiazol-2-yl)-2,5-diphenyltetrazolium bromide (MTT) assay under different treatment scenarios (control, 808 nm laser, IR820 with or without 808 nm laser, itraconazole, and IC/IR820 NPs with or without 808 nm laser). Under 808 nm laser, both IR820 and IC/IR820 NPs inhibited breast cancer cell viability in a dose-dependent manner (Fig. 2A–C). Specifically, the IC$_{50}$ values of IC/IR820 NPs (equivalent to IR820 and IC) are listed in Fig. S3A, while the corresponding IC50 values of free IR820 and IC was greater than 20 μM, respectively, indicating that the effect of IC/IR820 NPs may be significantly higher than that of PTT or IC alone. Without 808 nm laser, the suppression effect of free IR820 was very limited, but IC/IR820 NPs showed a significant inhibitory effect, indicating that IC/IR820 NPs may also be effective in the actual treatment of tumor sites that NIR cannot reach (Fig. S3B-D). In addition, IC/IR820 NPs (equivalent to 20 μM IR820 and 24 μM IC) showed a slightly higher inhibitory rate than that of free IC at the corresponding concentration, which may be due to enhanced intracellular uptake. Additionally, the results of colony formation assay (Fig. 2D–G, S3E-H), EdU assay (Fig. 2H–K, S3I-L), and LDH assay (Fig. 2L–N) were in agreement with that of MTT assay. Together, these results indicated the IC/IR820 NPs possesses excellent anti-tumor capability through combined chemo-phototherapeutic therapy in vitro.

3.3. Cytotoxicity of IC/IR820 NPs is dependent on ROS

Generating excessive ROS has been employed as a general therapeutic approach for cancer, including ROS-based nanomedicine [35–37]. However, several studies have reported that photothermal
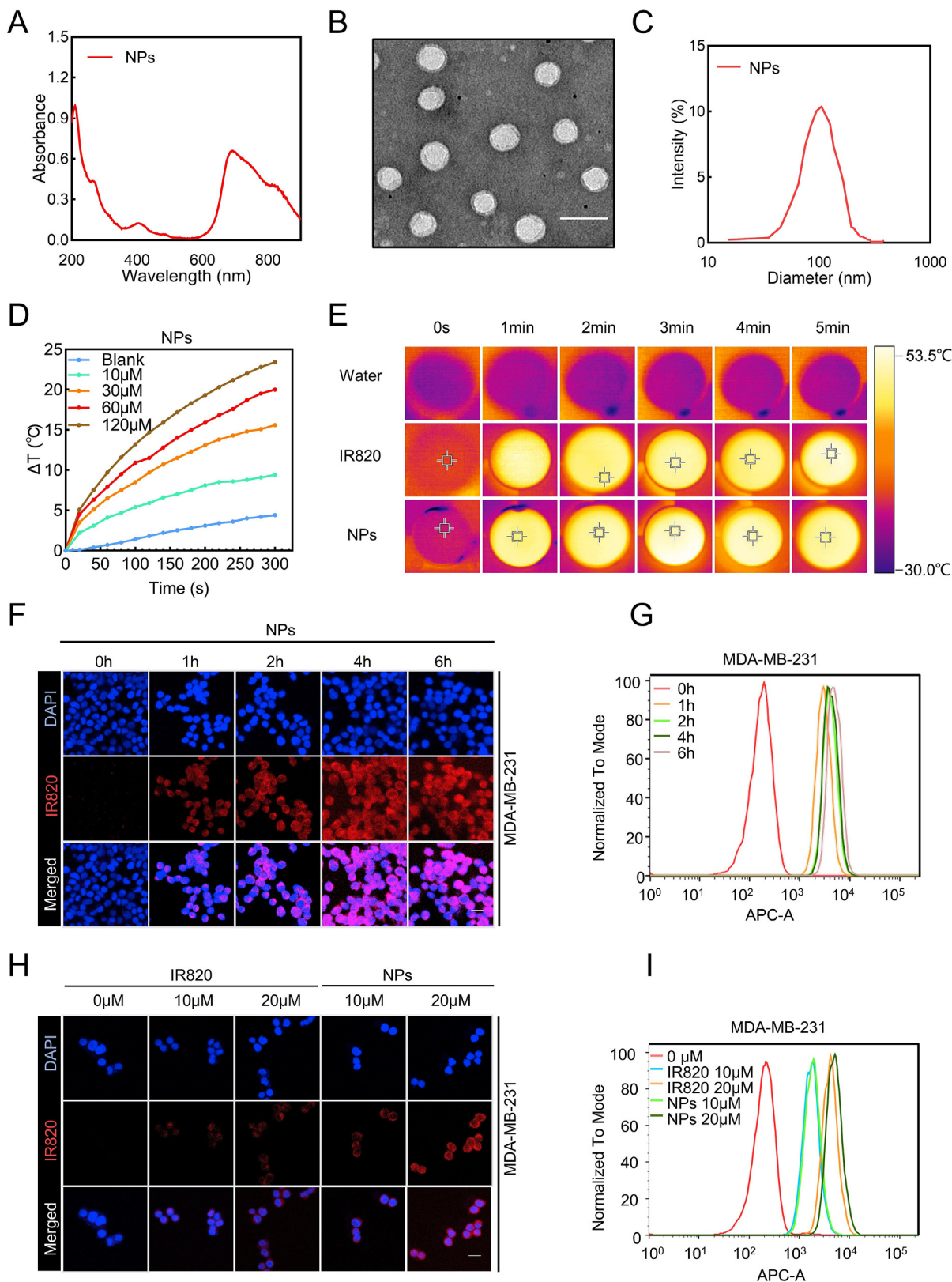
Fig. 1. Characterization and intercellular uptake of IC/IR820 NPs. (A) UV–vis absorption spectra of IC/IR820 NPs. (B) TEM image of IC/IR820 NPs. Scale bar: 100 nm. (C) Size distribution of IC/IR820 NPs. (D) Photothermal activity of IC/IR820 NPs dispersed in water at various concentrations ($\lambda = 808$ nm, P = 1.0 W/cm^2; irradiation time = 5 min). (E) Infrared thermal images of IR820 and IC/IR820 NPs in water after laser irradiation ($\lambda = 808$ nm, P = 1.0 W/cm^2; irradiation time = 5 min). (F) Fluorescence microscopy images and (G) flow cytometric results of cell uptake of IC/IR820 NPs into MDA-MB-231 cells at different time points. Scale bar: 20 μm. (H) Fluorescence microscopy images and (I) flow cytometric results of cell uptake of IR820 and IC/IR820 nanoparticles in MDA-MB-231 cells at different concentrations after incubation for 4 h. Scale bar: 20 μm.
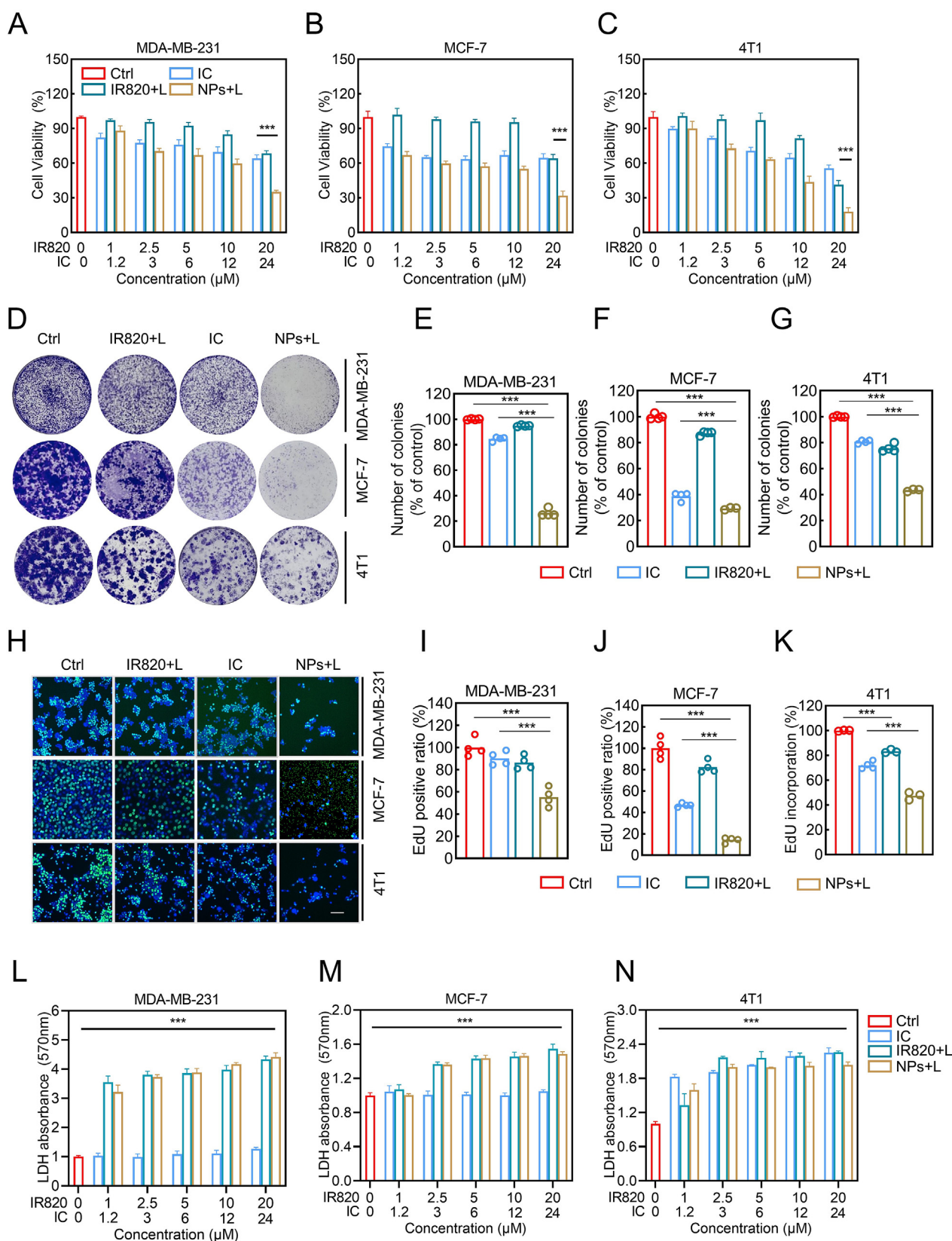
Fig. 2. The anti-breast cancer effect of IC/IR820 NPs. (A–C) Viability of MDA-MB-231, MCF-7, and 4T1 cells co-cultured with IC, IR820, and IC/IR820 nanoparticles. ($\lambda = 808$ nm, P $= 1.0$ W/cm^2; irradiation time $= 20$ s). (D–G) Representative images for colony formation of MDA-MB-231, MCF-7, and 4T1 cells co-cultured with IC, IR820, and IC/IR820 nanoparticles. ***$P < 0.001$. ($\lambda = 808$ nm, P $= 1.0$ W/cm^2; irradiation time $= 30$ s). (H–K) Quantification of MDA-MB-231, MCF-7, and 4T1 cells co-cultured with IC, IR820, and IC/IR820 nanoparticles in the EDU assay. Scale bar: 20 µm. ($\lambda = 808$ nm, P $= 1.0$ W/cm^2; irradiation time $= 20$ s). (L–N) LDH assay of MDA-MB-231, MCF-7, and 4T1 cells co-cultured with IC, IR820, and IC/IR820 nanoparticles. ($\lambda = 808$ nm, P $= 1.0$ W/cm^2; irradiation time $= 20$ s).

therapy-induced ROS is still insufficient to eliminate all cancer cells during treatment due to the limited penetration of NIR light irradiation [24,38]. Intriguingly, itraconazole has been reported to induce ROS in cancer cells and cause cell death [10,11,39]. Therefore, we speculated that the anti-tumor activity of IC/IR820 NPs might be dependent on excessive ROS levels. As mitochondria are the main source of cellular ROS, we used Mito-tracker and Lyso-tracker to verify the subcellular localization of IC/IR820 NPs. IC/IR820 NPs exhibited better colocalization with Mito-Tracker than free IR820. However, the colocalization of Lyso-Tracker did not show a difference between IC/IR820 NPs and IR820 (Fig. 3A–C, S4A-C). Then, the 2′,7′-dichlorofluorescein diacetate (DCFH-DA) probe was employed to assess the intracellular production of ROS to investigate whether a synergistic effect exists between itraconazole and IR820. IC/IR820 NPs under 808 nm laser exhibited a much stronger fluorescence intensity than IC and IR820 with or without 808 nm laser (Fig. 3D, E, S4D-G). These results were further validated by flow cytometry assay (Fig. 3F–H). Moreover, the high levels of ROS were associated with more potent cytotoxicity in breast cancer cells. The cellular inhibition ratio of IC/IR820 NPs could be rescued through treatment with N-acetyl cysteine (NAC), a small molecule inhibitor of ROS (Fig. 3I–K). These results indicated that IC/IR820 NPs enhance translocation to the mitochondria, resulting in excessive ROS released by the damaged mitochondria.

Cancer cells are equipped with robust antioxidant defenses to enable them to tolerate oxidative stress induced by high levels of ROS [40–42]. Therefore, we evaluated members of the antioxidant system using western blot. The expression of nuclear factor erythroid-derived 2-like 2 (NRF2) and superoxide dismutase 2 (SOD2) was significantly higher with IC/IR820 NPs under 808 nm laser than other treatments, which could be rescued with NAC (Fig. S4H-M).

3.4. IC/IR820 NPs trigger ROS-dependent apoptosis in breast cancer cells

Multiple lines of evidence indicate that excessive ROS may lead to apoptosis in cancer cells [43,44]. Annexin V-fluorescein isothiocyanate (FITC)/propidium iodide (PI) double staining assay was performed to explore the underlying molecular mechanisms of cell death mediated by IC/IR820 NPs. As illustrated in Fig. S5A-D, IC/IR820 NPs showed a significantly increased apoptotic percentage of cells compared to IR820 or itraconazole separately. The increased apoptotic rate after IC/IR820 NPs treatment was rescued with NAC treatment, indicating the regulatory role of ROS in IC/IR820 NPs-induced apoptosis (Fig. 4A–D). Consistently, the expression of apoptotic markers (e.g., cleaved-caspase 3, cleaved-PARP) can also be recovered after NAC treatment (Fig. 4E–G). When treated with ZVAD, an apoptosis inhibitor, breast cancer cells were significantly rescued from IC/IR820 NPs treatment (Fig. 4H–J). However, the recovery rates in different breast cancer cells were lower than with NAC treatment, suggesting that ROS-induced breast cancer cell death may include other mechanisms.

3.5. IC/IR820 NPs-mediated ROS induce cytotoxic autophagy in breast cancer cells

Previously, our group investigated cytotoxic autophagy induced by itraconazole in glioblastoma cells [45]. Furthermore, itraconazole has been gradually acknowledged as an inducer of autophagic cell death in other types of cancer cells [9,10,46]. Therefore, we attempted to explore whether IC/IR820 NPs induce autophagy in breast cancer cells. Indeed, microtubule-associated protein light chain 3 (LC3)-II accumulation was observed in response to IC/IR820 NPs treatment (Fig. S6A-C). Consistently, there was a prominent accumulation of LC3B puncta in IC/IR820 NPs-treated cells compared with other groups, as evidenced by LC3B immunofluorescence staining (Fig. S6D-I). ROS is a well-known inducer of autophagy [47–49]. Therefore, we explored whether ROS modulates autophagy in this context. Intriguingly, a marked reduction in the con-

version of LC3-I to LC3II and SQSTM1 was observed by immunoblotting (Fig. 5A–C) and immunofluorescent assays (Fig. 5D–G, S6J, K) after NAC treatment. Autophagy is considered as a double-edged sword for cell survival [50]. To assess the role of autophagy in IC/IR820 NPs-induced cell death, we pretreated the cells with autophagy inhibitor 3-MA, which rescued the inhibited cell viability after IC/IR820 NPs treatment (Fig. 5H–J). These results indicate that IC/IR820 NPs induce autophagic death in breast cancer cells.

Recent studies indicate the accumulation of autophagosomes may induce autophagic death [27]. Accumulation of autophagy-specific substrate SQSTM1 along with an increase in LC3B-II levels was observed in IC/IR820 NPs-treated cells, implying an impairment of autophagic flux (Fig. S6A-C). A tandem mRFP-GFP-tagged LC3B construct was used to determine whether the blocked autophagic flux resulted from a failure in autophagosome-lysosome fusion. As shown in Fig. 5K-M, a large proportion of LC3B puncta exhibited RFP$^+$GFP$^+$ signal (autophagosome) in IC/IR820 NPs group rather than RFP$^+$GFP$^-$ signal (autolysosome), suggesting that IC/IR820 NPs might block the fusion of the autophagosomes with the lysosomes. Together, our data indicate that IC/IR820 NPs induce ROS generation in breast cancer cells, leading to ROS-dependent apoptotic and autophagic cell death.

3.6. In vivo anti-breast cancer effects of IC/IR820 NPs

To further explore the biodistribution of IC/IR820 NPs, a live imaging system was utilized to monitor the fluorescence signal of IC/820 NPs at various time points (Fig. 6A). We found that both free IR820 and IC/IR820 NPs had reached maximum fluorescence after 4 h, so laser irradiation at 4 h after intravenous administration was chosen for subsequent PTT. Moreover, the attenuation of the fluorescence intensity of IC/IR820 NPs was much slower than that of free IR820 at tumor sites, and the fluorescence signal could last for 24 h. After 24 h, the tumor and major organs were excised to further explore the accumulation efficiency in the tumor site. As shown in Fig. S7A, there was a prolonged retention time of IC/IR820 NPs in the tumor site compared with free IR820, indicating that the EPR effect may promote the accumulation of IC/IR820 NPs at the tumor site.

Mice bearing orthotropic 4T1 tumors were injected with normal saline (NS), IC, IR820, IC/IR820 NPs every 2 days for 17 days via the tail vein to investigate the in vivo therapeutic effects (Fig. 6B). At 4 h after injection, the tumor was irradiated with 808 nm laser (1W cm^{-2}) for 5 min. It was clear that the IC/IR820 NPs group had an obvious temperature increase as the irradiation time was prolonged, approaching 43.8 °C at 5 min (Fig. 6C). Moreover, significantly enhanced anti-tumor effects of IC/IR820 NPs were verified in vivo. IC/IR820 NPs exhibited excellent therapeutic effect as evidenced by the visual observation of tumor tissues (Fig. 6D, S7B). As expected, the IC/IR820 NPs group displayed the smallest tumor volume and the highest tumor inhibition ratio among all groups (Fig. 6E–F). Specifically, the tumor inhibition ratio of NS, IC, IR820, IC/IR820 was around 0, 21%, 44%, and 90%, respectively. Moreover, no noticeable body weight loss was observed (Fig. 6G), indicating a good toxicity profile of the IC/IR820 NPs in mice.

Furthermore, the IC/IR820 NPs induced elevated oxidative damage, apoptosis, and autophagy, as well as decreased cell proliferation, as evidenced by stronger IHC staining of 8-OHdG, cleaved-caspase3 and LC3B, and weaker IHC staining of Ki-67 (Fig. 6H-L). H&E staining showed no detectable pathological damage for the main organs following IC/IR820 NPs treatment (Fig. S7C). Serum biochemical analysis, including alanine aminotransferase and aspartate aminotransferase (ALT/AST) and blood urea nitrogen, and creatinine (BUN/CR), are commonly used to reflect the function of the liver and kidney, respectively. We found that these indexes were within their normal range and had no significant fluctuation among all groups, suggesting low side-effects of the IC/IR820 NPs (Fig. S7D-G).
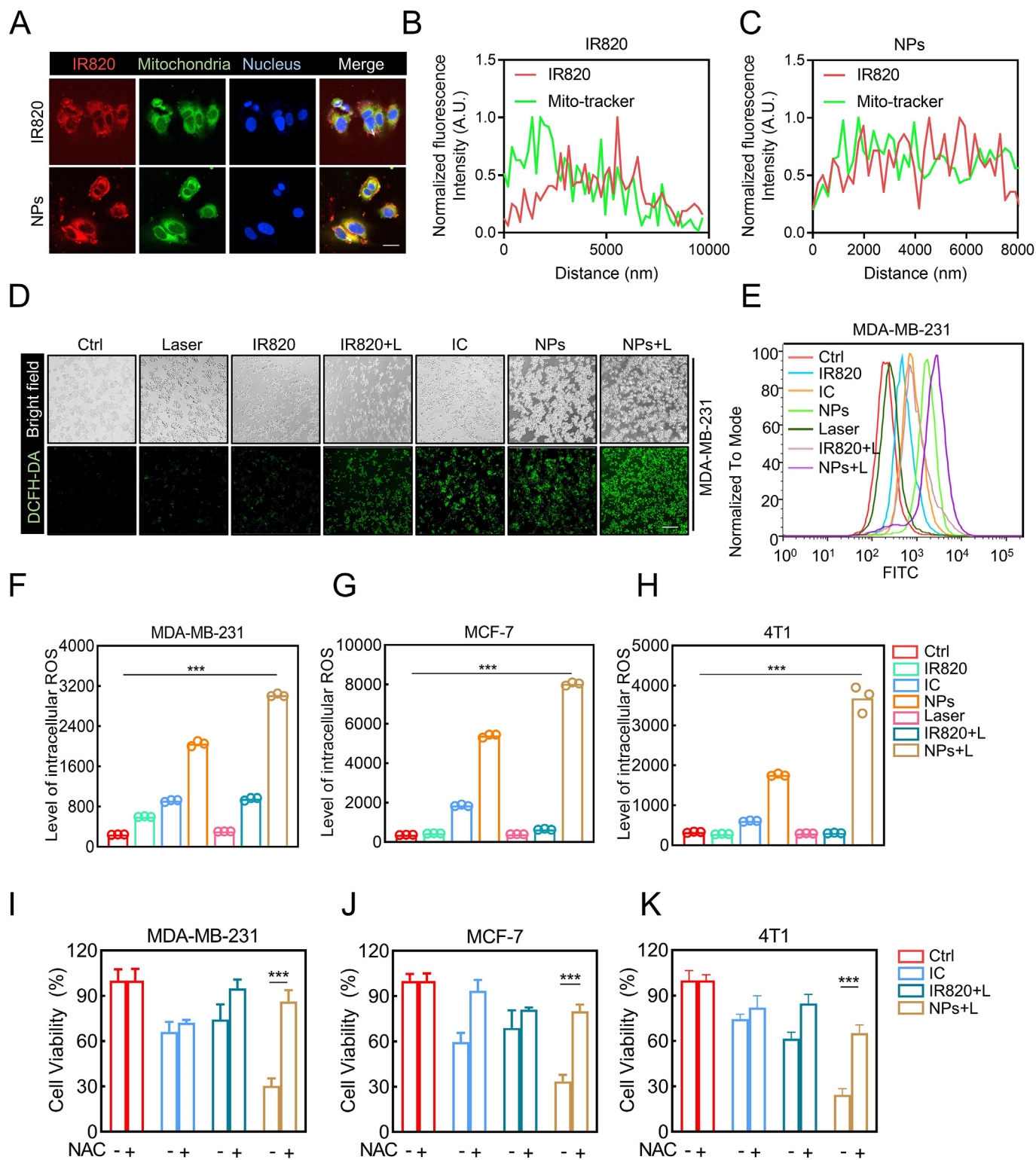
Fig. 3. IC/IR820 NPs-mediated ROS induce breast cancer cell death. (A–C) Immunofluorescence images to show subcellular localization of IR820 and IC/IR820 NPs. Scale bar: 20 μm. (D) Fluorescence microscopy images and (E) flow cytometry analysis for intracellular ROS generation of MDA-MB-231 cells using DCFH-DA as a probe. Scale bar: 20 μm. (λ = 808 nm, P = 1.0 W/cm^2; irradiation time = 2 min). (F–H) Flow cytometry statistical analysis for intracellular ROS generation of MDA-MB-231, MCF-7 and 4T1 cells using DCFH-DA as a probe. Scale bar: 20 μm. (λ = 808 nm, P = 1.0 W/cm^2; irradiation time = 2 min). (I–K) Viability of specific groups with or without NAC treatment in MDA-MB-231, MCF-7 and 4T1 cells. (λ = 808 nm, P = 1.0 W/cm^2; irradiation time = 20 s).

3.7. IC/IR820 NPs inhibit metastasis of breast cancer cells
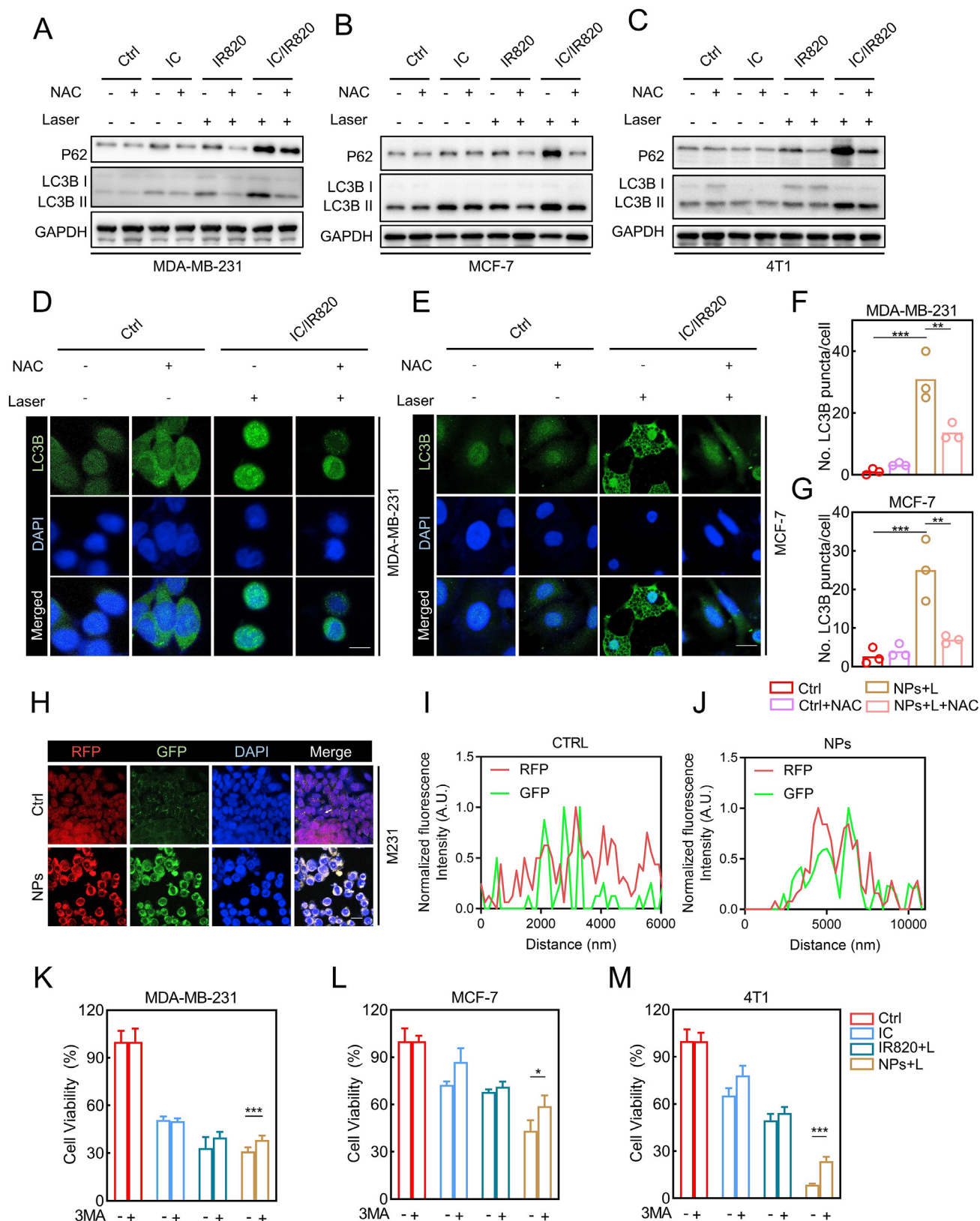
Metastasis is considered as one of the primary reasons leading to a worse survival rate in breast cancer patients [51,52]. The lung and liver are generally accepted as the primary target sites of breast cancer metastasis [53]. In recent years, nanoparticle-based drug delivery systems have been utilized extensively to inhibit tumor metastasis [54,55]. The impact of IC/IR820 NPs on breast cancer metastasis was therefore
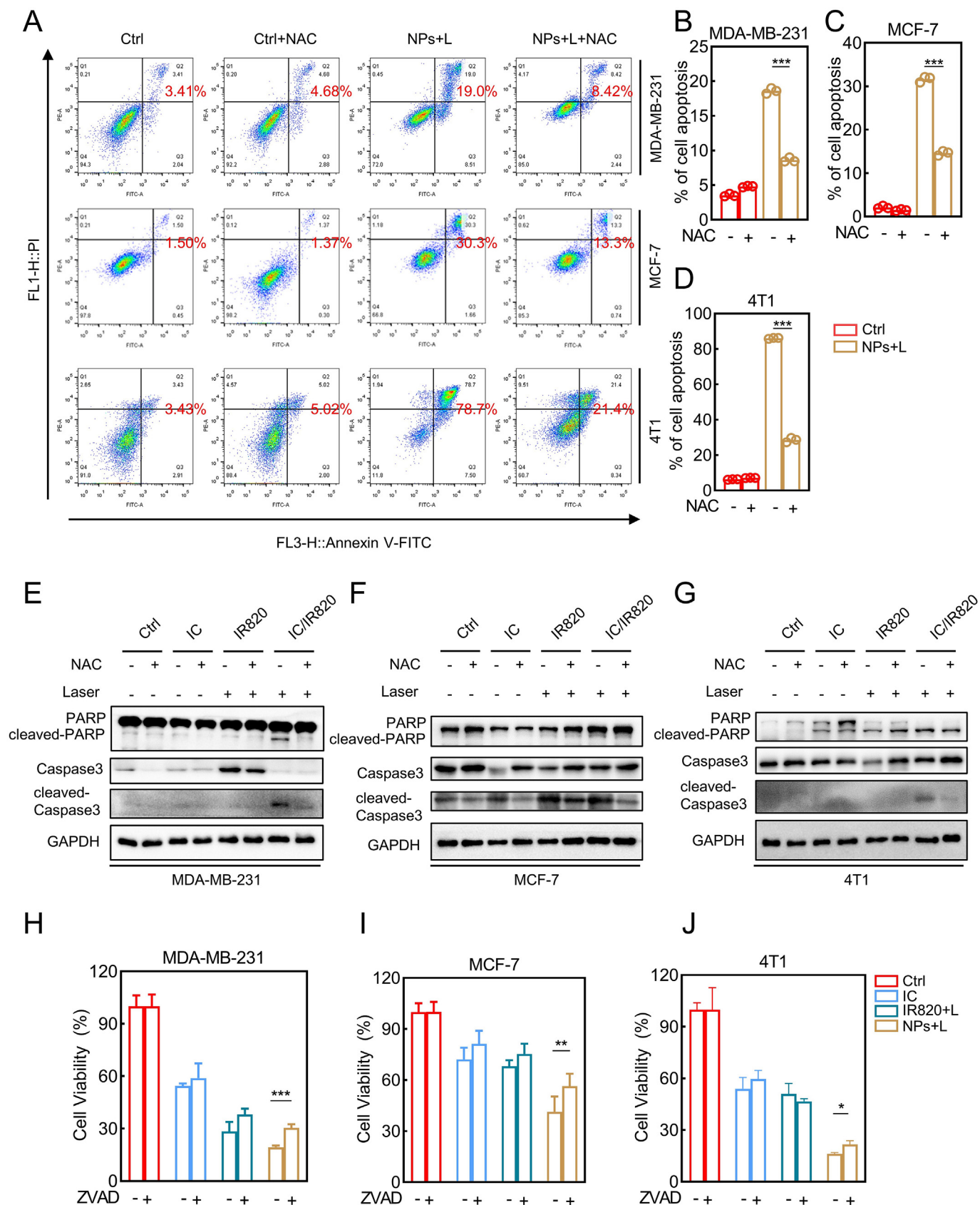
Fig. 4. IC/IR820 NPs trigger ROS-dependent apoptosis in breast cancer cells. (A–D) Apoptosis of IR820, IC, and IC/IR820 NPs were evaluated by annexin V-FITC/PI staining in MDA-MB-231, MCF-7 and 4T1 cells, quantification of apoptotic cell ratio. (λ = 808 nm, P = 1.0 W/cm^2; the irradiation time = 2 min). (E–G) Immunoblot analysis of apoptotic markers for MDA-MB-231, MCF-7 and 4T1 cells treated IC, IR820, IC/IR820 with or without NAC treatment. (λ = 808 nm, P = 1.0 W/cm^2; irradiation time = 2 min). (H–J) Viability of specific groups with or without ZVAD treatment in MDA-MB-231, MCF-7 and 4T1 cells. (λ = 808 nm, P = 1.0 W/cm^2; irradiation time = 20 s).

Fig. 5. IC/IR820 NPs-mediated ROS induce autophagic cell death in breast cancer cells. (A–C) Immunoblot analysis of autophagic markers for MDA-MB-231, MCF-7 and 4T1 cells treated IC, IR820, IC/IR820 with or without NAC treatment. ($\lambda = 808$ nm, $P = 1.0$ W/cm^2; irradiation time = 2 min). (D–G) Immunofluorescence assays display subcellular localization of LC3B puncta in MDA-MB-231 and MCF-7 cells treated IC/IR820 NPs with or without NAC treatment, quantification of LC3B puncta per cell. Scale bar: 10 μm. ($\lambda = 808$ nm, $P = 1.0$ W/cm^2; irradiation time = 30s). (H–J) Immunofluorescence images to show subcellular localization of LC3-GFP and LC3-RFP. Scale bar: 20 μm. (K–M) Viability of specific groups with or without 3 MA treatment in MDA-MB-231, MCF-7 and 4T1 cells. ($\lambda = 808$ nm, $P = 1.0$ W/cm^2; irradiation time = 20 s).
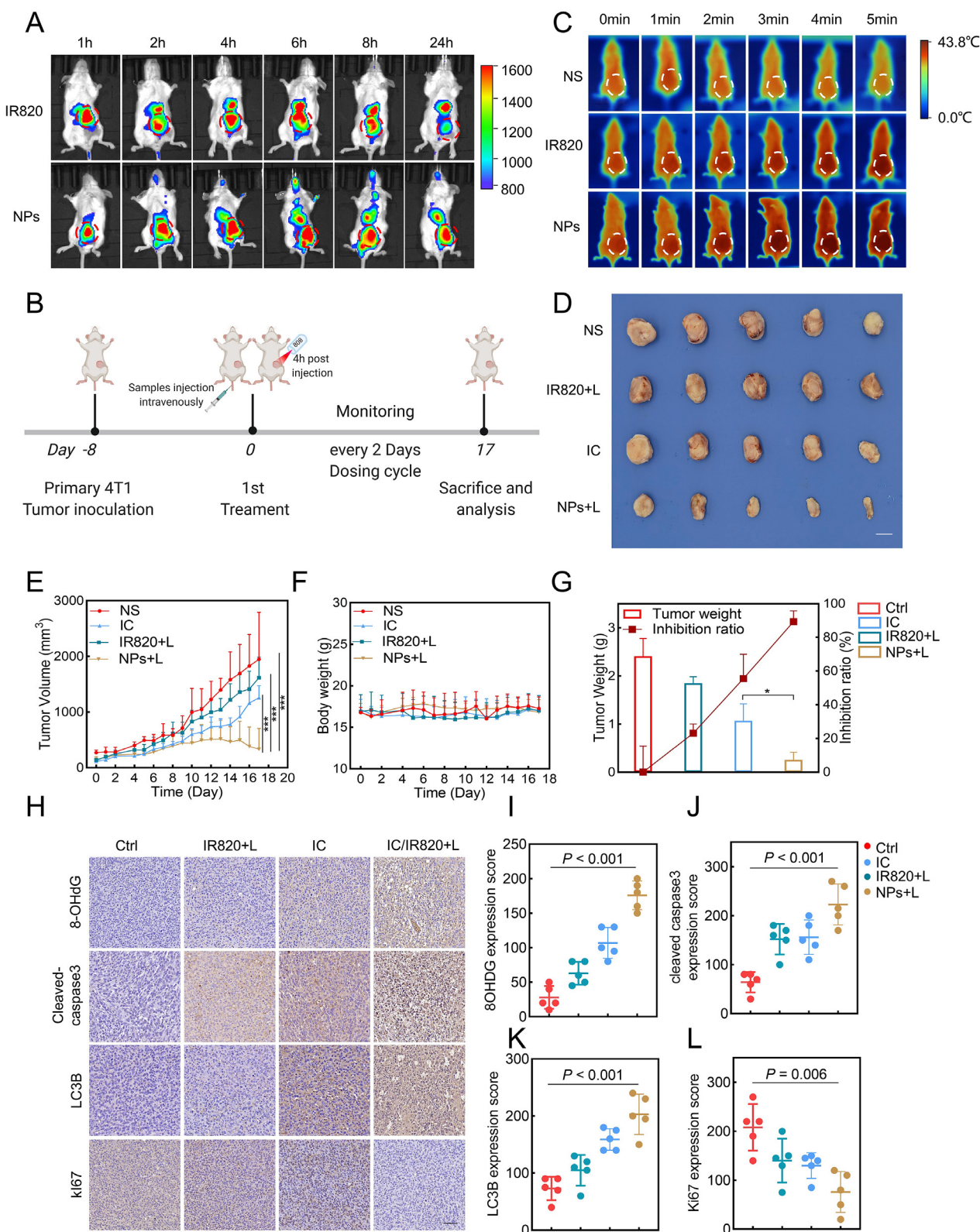
Fig. 6. The anti-breast cancer effect of IC/IR820 NPs *in vivo*. (A) *In vivo* distribution of IR820 and IC/IR820 NPs at different times. (B) Schematic illustration of the procedure of tumor treatment *in vivo*. Created with BioRender.com. (C) *In vivo* thermal imaging of different groups of treated mice. (λ = 808 nm, P = 1.0 W/cm²; irradiation time = 5 min). (D) Representative images of isolated tumors. Scale bar: 1 cm. (E) The volume of tumors from each group (5 mice per group) was measured at the indicated time points. (F) The body weight of mice in each group was measured at the indicated time points. (G) The weight of individual tumors and the inhibition rate. (H–L) Representative immunohistochemistry images of mice treated with vehicle, IR820, or IC/IR820 NPs intravenously through tail vein at the indicated time points, quantification of Ki67, 8-OHDG, cleaved-caspase 3, and LC3B expression score. Scale bar: 50 μm. (λ = 808 nm, P = 1.0 W/cm²; irradiation time = 5 min).
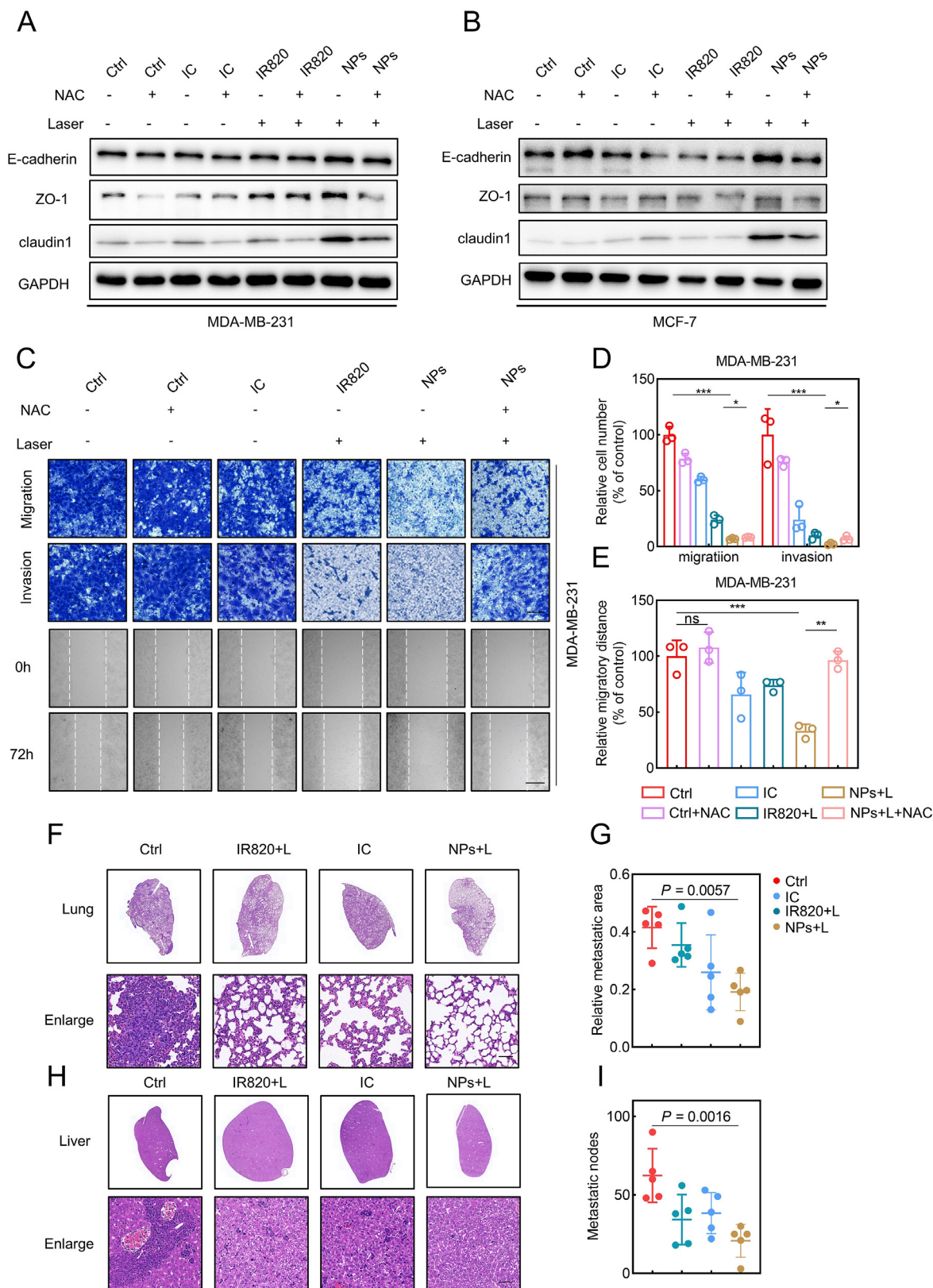
Fig. 7. IC/IR820 NPs inhibit breast cancer metastasis. (A–B) Immunoblot analysis of EMT markers for MDA-MB-231 and MCF-7 cells treated with IC, IR820, IC/IR820 with or without NAC treatment/irradiation (808 nm, 1.0 W cm^{-2}, 20 s). (C–E) Representative images of migration, invasion, and scratch test of MDA-MB-231 cells, quantification of migration/invasion cell number and migratory distance. Scale bar for migration and invasion assay: 50 μm. Scale bar for scratch test: 20 μm. (F–I) Representative lung, liver H&E staining of mice bearing 4T1 orthotopic breast tumor xenografts treated with vehicle, IR820 + Laser, IC, IC/IR820 NPs + Laser at the end of the treatment period. Quantification of the relative metastatic area in lungs and metastatic nodes in livers. Scale bar: 50 μm.
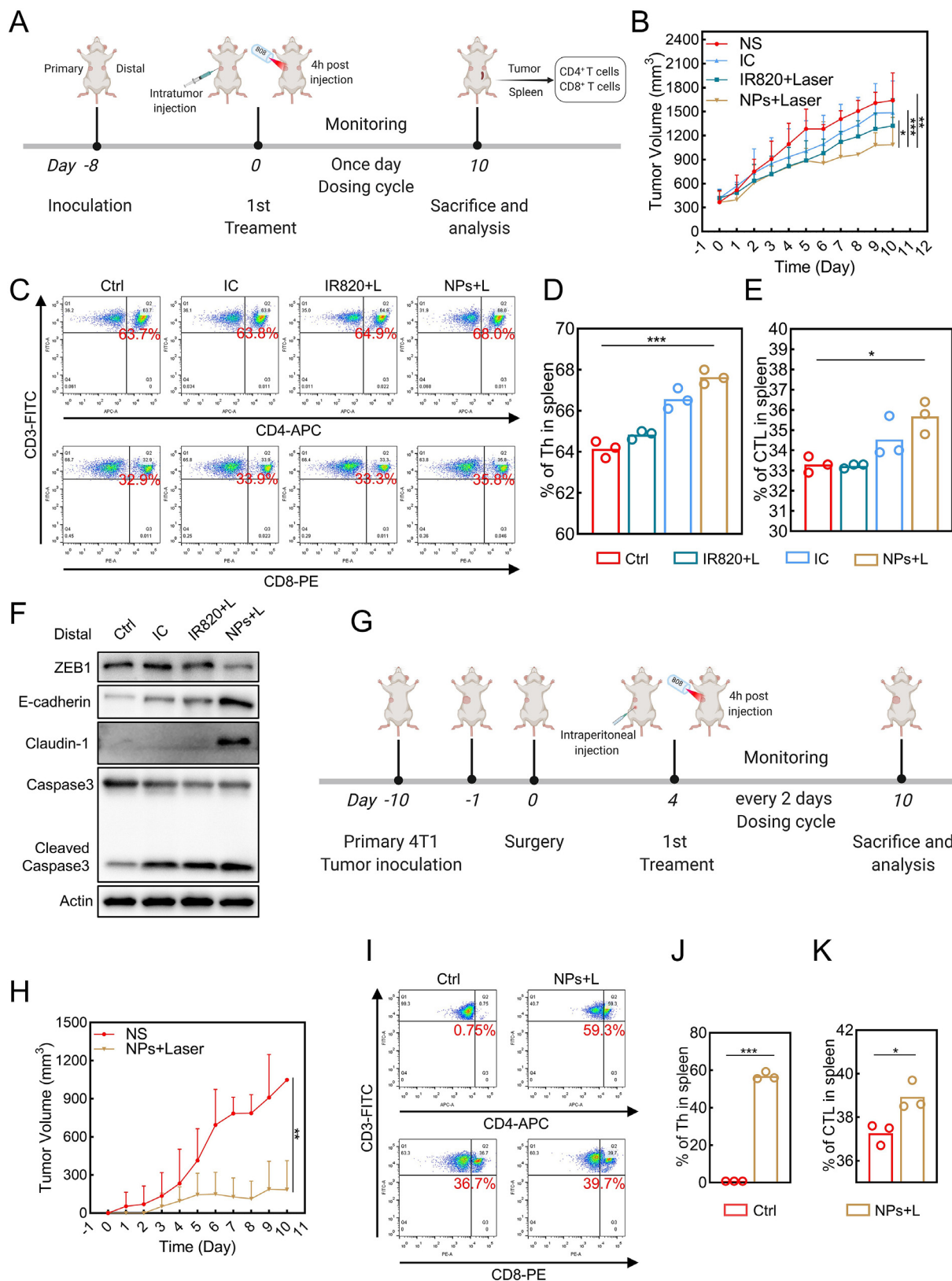
Fig. 8. IC/IR820 NPs induce immune response and inhibit recurrence in mouse model. (A) Schematic illustration of the treatment of bilateral tumors. Created with BioRender.com. (B) Distant tumor volumes. (C–E) Representative results of CD4+ T cells and CD8+ T cells. Quantification of percentage of CD4+ T cells and CD8+ T cells in the spleen. (F) Immunoblot analysis of E-cadherin, caspase3, cleaved-caspase3 for distal tumor treated with NS, IC, IR820, and IC/IR820 NPs. (G) Schematic illustration of the treatment of postsurgical mice. Created with BioRender.com. (H) Tumor volumes. (I–K) Representative results of CD4+ T cells and CD8+ T cells. Quantification of percentage of CD4+ T cells and CD8+ T cells in the spleen.

investigated. IC/IR820 NPs promoted expression levels of epithelial markers, including E-cadherin, ZO1, and Claudin-1, which can be rescued through NAC treatment (Fig. 7A–B). In agreement, IC/IR820 NPs significantly inhibited migration and invasion of breast cancer cells (Fig. 7C–E, S8). The effect of IC/IR820 NPs on breast cancer metastasis was then evaluated in the 4T1 orthotropic mammary tumor metastasis model. Consistent with the *in vitro* results, the formation of the metastatic area in the lung or liver was significantly reduced after IC/IR820 NPs treatment compared with other groups (Fig. 7F–I). Taken together, these results suggest that IC/IR820 NPs inhibit breast cancer metastasis *in vitro* and *in vivo*.

3.8. Immune response and anti-relapse ability induced by IC/IR820 nanoparticles

It has been reported that PTT may result in immunogenic cell death (ICD), triggering an anti-tumor immune response [56]. In addition, recent studies indicate that autophagy may induce immune response through activation of antigen-presenting cells, including dendritic cells, suggesting itraconazole may participate in immune response [16,57]. In order to investigate the immune response caused by IC/IR820 NPs treatment in the mouse model, we next constructed a bilateral subcutaneous 4T1 model (Fig. 8A). As expected, IC/IR820 NPs showed a better distant and primary tumor inhibition ratio on account of the photo-chemotherapy and activated anti-tumor immunity (Fig. 8B, S9A-B). Furthermore, significant infiltration and upregulation of CD4$^+$ and CD8$^+$ T cells within spleen and tumors were detected, respectively, thus validating the systemic immune response triggered by IC/IR820 NPs (Fig. 8C–E, Fig. S8C-E). Epithelial markers, including E-cadherin, were upregulated abundantly in primary and distal tumors treated with IC/IR820 NPs under 808 nm laser (Fig. 8F, S9F). Therefore, the IC/IR820 NPs could effectively inhibit distant breast cancer spread by triggering an immune response due to an increased proportion of CD4$^+$, CD8$^+$ T cells.

Recurrence can occur after breast-conserving surgery, especially following incomplete resection, contributing to the poor prognosis of late-stage breast cancer [58]. A surgical model on 4T1 bearing mice was built to evaluate the efficacy of IC/IR820 NPs in preventing postsurgical recurrence (Fig. 8G, S8G-H). As shown in Fig. 8H, mice treated with IC/IR820 NPs had an enhanced anti-recurrency capability compared with the NS group. Moreover, there was no obvious toxicity since there were no significant changes in body weight (Fig. S9I). Additionally, proteins associated with apoptosis and metastasis were also investigated (Fig. 8I–K, S9J-M). These data show that IC/IR820 NPs have excellent potential for activating anti-tumor immunity and preventing postsurgical recurrence.

4. Conclusion

In this study, we performed co-assembly of itraconazole and IR820 for the first time through the film dispersion method, which solved the poor water solubility of itraconazole and improved the efficacy of photothermal therapy. Itraconazole has excellent antitumor activity in tumor therapy, but its solubility in water is only 1–4 ng/mL, which hinders its clinical application [18]. At present, some researchers have improved the solubility of itraconazole to a certain extent by developing new crystal forms, using membrane emulsification, spray drying, and other technologies [59,60]. However, its cost and complexity have hindered its widespread adoption. The thin-film dispersion method studied in this paper can rapidly assemble itraconazole and IR820 with pure drug molecules [61,62]. Itraconazole can be efficiently and easily formed into a dosage form in an aqueous solution, which has obvious advantages for subsequent rapid production and clinical application.

Photothermal therapy has the advantages of non-invasiveness and high efficiency in clinical use, which relies on the irradiation of photothermal agents with specific wavelengths of the laser [19]. The penetration of the laser is relatively limited. It is reported that the effective

excitation intensity of laser is significantly attenuated within a few centimeters of the human body. Therefore, photothermal therapy is usually used for superficial tumors, including melanoma and breast cancer [24]. Although breast cancer is often considered a superficial tumor, its depth can still reach more than 10 cm, and the laser may not be sufficient to kill cancer cells completely. Due to the lack of targeting design, photothermal agents are evenly distributed in the body after entering the human body, which may cause side effects to the human body. The solution proposed by our research can solve this problem. By forming nanoparticles, photothermal agents and drugs can passively target tumor tissues through the EPR effect, which may reduce the toxicity to normal cells. In addition, itraconazole and photothermal agents can display a synergistic effect on tumor suppression. Itraconazole can generate a large amount of ROS, killing tumors through apoptosis and autophagic death, as well as inhibiting the Hedgehog pathway [9,13]. Moreover, immunogenic death and itraconazole-mediated autophagy may promote the immune presentation of tumor antigens and enhance the immune killing of tumors [16,63].

In this study, IC/IR820 nanoparticles induced ROS-mediated apoptosis and autophagic death, as well as their therapeutic effects on breast cancer metastasis, tumor immunity, and recurrence. NAC restored the expression level of EMT markers in breast cancer cells, suggesting that ROS is involved in regulating the EMT signaling pathway, which may be related to itraconazole-regulated Hedgehog pathway. But the molecular mechanism needs to be further explored in the future. At the same time, the molecular mechanism of itraconazole-mediated immune synergy on tumors needs further investigation. These explorations are of significance for the improvement of itraconazole in the treatment of breast cancer and other tumors.

In summary, we have successfully synthesized IC/IR820 NPs using a minimalist and robust film dispersion method, which overcomes the shortcomings and enhances the advantages of both IR820 and itraconazole. The properties of the nanoparticles improved the targeting and uptake of IR820 and enhanced itraconazole solubility. The IC/IR820 NPs were capable of inducing oxidative stress-induced apoptosis, autophagic death, and immunogenic death, which effectively inhibited breast cancer metastasis and recurrence. These findings may help develop reasonable and effective strategies for the clinical treatment of breast cancer, which may facilitate the clinical translation of nano-delivered drugs.

Credit author statement

Hui Ming: Writing – original draft; Conceptualization; Investigation; Data curation. **Bowen Li**: Writing – original draft; Visualization; Conceptualization; Methodology. **Hailong Tian**: Writing – review & editing; Conceptualization; Methodology; Validation; Project administration. **Li Zhou**: Writing – review & editing; Methodology. **Jingwen Jiang**: Writing – review & editing; Methodology. **Tingting Zhang**: Investigation; Resources. **Ling Qiao**: Investigation; Resources. **Peijie Wu**: Investigation. **Edouard C. Nice**: Writing – review & editing. **Wei Zhang**: Funding acquisition. **Weifeng He**: Writing – review & editing; Project administration. **Canhua Huang**: Funding acquisition; Writing – review & editing. **Haiyuan Zhang**: Writing – review & editing; Supervision.

Declaration of competing interest

The authors declare that they have no known competing financial interests or personal relationships that could have appeared to influence the work reported in this paper.

1·3·5 project for disciplines of excellence, West China Hospital, Sichuan University (ZYJC21004).

Appendix A. Supplementary data

Supplementary data to this article can be found online at https://doi.org/10.1016/j.mtbio.2022.100289.

References

[1] H. Sung, J. Ferlay, R.L. Siegel, M. Laversanne, I. Soerjomataram, A. Jemal, F. Bray, Global cancer statistics 2020: GLOBOCAN estimates of incidence and mortality worldwide for 36 cancers in 185 countries, CA A Cancer J. Clin. 71 (2021) 209–249.

[2] R.L. Siegel, K.D. Miller, H.E. Fuchs, A. Jemal, Cancer statistics, CA A Cancer J. Clin. 71 (2021) 7–33, 2021.

[3] A.G. Waks, E.P. Winer, Breast cancer treatment: a review, Jama 321 (2019) 288–300.

[4] S.J.A. Buczacki, S. Popova, E. Biggs, C. Koukorava, J. Buzzelli, L. Vermeulen, L. Hazelwood, H. Francies, M.J. Garnett, D.J. Winton, Itraconazole targets cell cycle heterogeneity in colorectal cancer, J. Exp. Med. 215 (2018) 1891–1912.

[5] R.J. Kelly, A.M. Ansari, T. Miyashita, M. Zahurak, F. Lay, A.K. Ahmed, L.J. Born, M.K. Pezhouh, K.J. Salimian, C. Ng, A.E. Matsangos, A.H. Stricker-Krongrad, K.I. Mukaisho, G.P. Marti, C.H. Chung, M.I. Canto, M.A. Rudek, S.J. Meltzer, J.W. Harmon, Targeting the Hedgehog pathway using itraconazole to prevent progression of barrett's esophagus to invasive esophageal adenocarcinoma, Ann. Surg. 273 (2021) e206–e213.

[6] D.E. Gerber, W.C. Putnam, F.J. Fattah, K.H. Kernstine, R.A. Brekken, I. Pedrosa, R. Skelton, J.M. Saltarski, R.E. Lenkinski, R.D. Leff, C. Ahn, C. Padmanabhan, V. Chembukar, S. Kasiri, R.R. Kallem, I. Subramaniyan, Q. Yuan, Q.N. Do, Y. Xi, S.I. Reznik, L. Pelosof, B. Faubert, R.J. DeBerardinis, J. Kim, Concentration-dependent early antivascular and antitumor effects of itraconazole in non-small cell lung cancer, Clin. Cancer Res. : Off. J. Am. Assoc. Canc. Res. 26 (2020) 6017–6027.

[7] S. Takahashi, M. Karayama, M. Takahashi, J. Watanabe, H. Minami, N. Yamamoto, I. Kinoshita, C.C. Lin, Y.H. Im, I. Achiwa, E. Kamiyama, Y. Okuda, C. Lee, Y.J. Bang, Pharmacokinetics, safety, and efficacy of trastuzumab deruxtecan with concomitant ritonavir or itraconazole in patients with HER2-expressing advanced solid tumors, Clin. Cancer Res. : Off. J. Am. Assoc. Canc. Res. 27 (2021) 5771–5780.

[8] Q. Hu, Y.C. Hou, J. Huang, J.Y. Fang, H. Xiong, Itraconazole induces apoptosis and cell cycle arrest via inhibiting Hedgehog signaling in gastric cancer cells, J. Exp. Clin. Cancer Res. 36 (2017) 50.

[9] H. Deng, L. Huang, Z. Liao, M. Liu, Q. Li, R. Xu, Itraconazole inhibits the Hedgehog signaling pathway thereby inducing autophagy-mediated apoptosis of colon cancer cells, Cell Death Dis. 11 (2020) 539.

[10] X. Wang, S. Wei, Y. Zhao, C. Shi, P. Liu, C. Zhang, Y. Lei, B. Zhang, B. Bai, Y. Huang, H. Zhang, Anti-proliferation of breast cancer cells with itraconazole: Hedgehog pathway inhibition induces apoptosis and autophagic cell death, Cancer Lett. 385 (2017) 128–136.

[11] W. Wang, X. Dong, Y. Liu, B. Ni, N. Sai, L. You, M. Sun, Y. Yao, C. Qu, X. Yin, J. Ni, Itraconazole exerts anti-liver cancer potential through the Wnt, PI3K/AKT/mTOR, and ROS pathways, Biomed. Pharmacother. 131 (2020) 110661.

[12] P. Pantziarka, V. Sukhatme, G. Bouche, L. Meheus, V.P. Sukhatme, Repurposing drugs in oncology (ReDO)-itraconazole as an anti-cancer agent, Ecancermedicalscience 9 (2015) 521.

[13] J. Kim, B.T. Aftab, J.Y. Tang, D. Kim, A.H. Lee, M. Rezaee, J. Kim, B. Chen, E.M. King, A. Borodovsky, G.J. Riggins, E.H. Epstein Jr., P.A. Beachy, C.M. Rudin, Itraconazole and arsenic trioxide inhibit Hedgehog pathway activation and tumor growth associated with acquired resistance to smoothened antagonists, Cancer Cell 23 (2013) 23–34.

[14] D. Neelakantan, H. Zhou, M.U.J. Oliphant, X. Zhang, L.M. Simon, D.M. Henke, C.A. Shaw, M.F. Wu, S.G. Hilsenbeck, L.D. White, M.T. Lewis, H.L. Ford, EMT cells increase breast cancer metastasis via paracrine GLI activation in neighbouring tumour cells, Nat. Commun. 8 (2017) 15773.

[15] C. Brenner, L. Galluzzi, O. Kepp, G. Kroemer, Decoding cell death signals in liver inflammation, J. Hepatol. 59 (2013) 583–594.

[16] C. Münz, Autophagy beyond intracellular MHC class II antigen presentation, Trends Immunol. 37 (2016) 755–763.

[17] M.S. Ally, K. Ransohoff, K. Sarin, S.X. Atwood, M. Rezaee, I. Bailey-Healy, J. Kim, P.A. Beachy, A.L. Chang, A. Oro, J.Y. Tang, A.D. Colevas, Effects of combined treatment with arsenic trioxide and itraconazole in patients with refractory metastatic basal cell carcinoma, JAMA Dermatol 152 (2016) 452–456.

[18] R.K. Mehta, D. Jakhar, I. Kaur, An office-based evaluation of various itraconazole brands, J. Am. Acad. Dermatol. 80 (2019) e113–e114.

[19] Y. Liu, P. Bhattarai, Z. Dai, X. Chen, Photothermal therapy and photoacoustic imaging via nanotheranostics in fighting cancer, Chem. Soc. Rev. 48 (2019) 2053–2108.

[20] X. Li, J.F. Lovell, J. Yoon, X. Chen, Clinical development and potential of photothermal and photodynamic therapies for cancer, Nat. Rev. Clin. Oncol. 17 (2020) 657–674.

[21] J. Chen, C. Ning, Z. Zhou, P. Yu, Y. Zhu, G. Tan, C. Mao, Nanomaterials as photothermal therapeutic agents, Prog. Mater. Sci. 99 (2019) 1–26.

[22] H. Dai, X. Wang, J. Shao, W. Wang, X. Mou, X. Dong, NIR-II organic nanotheranostics for precision oncotherapy, Small 17 (2021), e2102646.

[23] Y. Cai, W. Si, W. Huang, P. Chen, J. Shao, X. Dong, Organic dye based nanoparticles for cancer phototheranostics, Small 14 (2018), e1704247.

[24] X. Deng, Z. Shao, Y. Zhao, Solutions to the drawbacks of photothermal and photodynamic cancer therapy, Adv. Sci. 8 (2021) 2002504.

[25] W. Li, J. Peng, L. Tan, J. Wu, K. Shi, Y. Qu, X. Wei, Z. Qian, Mild photothermal therapy/photodynamic therapy/chemotherapy of breast cancer by Lyp-1 modified Docetaxel/IR820 Co-loaded micelles, Biomaterials 106 (2016) 119–133.

[26] L. Huang, Y. Li, Y. Du, Y. Zhang, X. Wang, Y. Ding, X. Yang, F. Meng, J. Tu, L. Luo, C. Sun, Mild photothermal therapy potentiates anti-PD-L1 treatment for immunologically cold tumors via an all-in-one and all-in-control strategy, Nat. Commun. 10 (2019) 4871.

[27] J. Jiang, L. Zhang, H. Chen, Y. Lei, T. Zhang, Y. Wang, P. Jin, J. Lan, L. Zhou, Z. Huang, B. Li, Y. Liu, W. Gao, K. Xie, L. Zhou, E.C. Nice, Y. Peng, Y. Cao, Y. Wei, K. Wang, C. Huang, Regorafenib induces lethal autophagy arrest by stabilizing PSAT1 in glioblastoma, Autophagy 16 (2020) 106–122.

[28] P. Jin, J. Jiang, N. Xie, L. Zhou, Z. Huang, L. Zhang, S. Qin, S. Fu, L. Peng, W. Gao, B. Li, Y. Lei, E.C. Nice, C. Li, J. Shao, K. Xie, MCT1 relieves osimertinib-induced CRC suppression by promoting autophagy through the LKB1/AMPK signaling, Cell Death Dis. 10 (2019) 615.

[29] S.A. Popova, S.J.A. Buczacki, Itraconazole perturbs colorectal cancer dormancy through SUFU-mediated WNT inhibition, Mol. Cell. Oncol. 5 (2018), e1494950.

[30] T. Sun, Y.S. Zhang, B. Pang, D.C. Hyun, M. Yang, Y. Xia, Engineered nanoparticles for drug delivery in cancer therapy, Angew Chem. Int. Ed. Engl. 53 (2014) 12320–12364.

[31] C. Lescop, Coordination-driven syntheses of compact supramolecular metallacycles toward extended metallo-organic stacked supramolecular assemblies, Acc. Chem. Res. 50 (2017) 885–894.

[32] J. He, C. Li, L. Ding, Y. Huang, X. Yin, J. Zhang, J. Zhang, C. Yao, M. Liang, R.P. Pirraco, J. Chen, Q. Lu, R. Baldridge, Y. Zhang, M. Wu, R.L. Reis, Y. Wang, Tumor targeting strategies of smart fluorescent nanoparticles and their applications in cancer diagnosis and treatment, Adv. Mater. 31 (2019), e1902409.

[33] J. Park, Y. Choi, H. Chang, W. Um, J.H. Ryu, I.C. Kwon, Alliance with EPR effect: combined strategies to improve the EPR effect in the tumor microenvironment, Theranostics 9 (2019) 8073–8090.

[34] R. Liu, W. Xiao, C. Hu, R. Xie, H. Gao, Theranostic size-reducible and no donor conjugated gold nanocluster fabricated hyaluronic acid nanoparticle with optimal size for combinational treatment of breast cancer and lung metastasis, J. Contr. Release 278 (2018) 127–139.

[35] B. Yang, Y. Chen, J. Shi, Reactive oxygen species (ROS)-Based nanomedicine, Chem. Rev. 119 (2019) 4881–4985.

[36] S. Kwon, H. Ko, D.G. You, K. Kataoka, J.H. Park, Nanomedicines for reactive oxygen species mediated approach: an emerging paradigm for cancer treatment, Acc. Chem. Res. 52 (2019) 1771–1782.

[37] Z. Zhang, S. Qin, Y. Chen, L. Zhou, M. Yang, Y. Tang, J. Zuo, J. Zhang, A. Mizokami, E.C. Nice, H.N. Chen, C. Huang, X. Wei, Inhibition of NPC1L1 disrupts adaptive responses of drug-tolerant persister cells to chemotherapy, EMBO Mol. Med. (2022), e14903.

[38] J.J. Fu, C.W. Li, Y. Liu, M.Y. Chen, Q. Zhang, X.Y. Yu, B. Wu, J.X. Li, L.R. Du, Y.Y. Dang, D. Wu, M.Y. Wei, Z.Q. Lin, X.P. Lei, The microneedles carrying cisplatin and IR820 to perform synergistic chemo-photodynamic therapy against breast cancer, J. Nanobiotechnol. 18 (2020) 146.

[39] E. Shekhova, O. Kniemeyer, A.A. Brakhage, Induction of mitochondrial reactive oxygen species production by itraconazole, terbinafine, and amphotericin B as a mode of action against Aspergillus fumigatus, Antimicrob. Agents Chemother. 61 (2017).

[40] D.B. Fox, N.M.G. Garcia, B.J. McKinney, R. Lupo, L.C. Noteware, R. Newcomb, J. Liu, J.W. Locasale, M.D. Hirschey, J.V. Alvarez, NRF2 activation promotes the recurrence of dormant tumour cells through regulation of redox and nucleotide metabolism, Nat. Metab. 2 (2020) 318–334.

[41] L. Peng, J. Jiang, H.N. Chen, L. Zhou, Z. Huang, L. Zhang, S. Qin, P. Jin, M. Luo, B. Li, J. Shi, N. Xie, L.W. Deng, Y.C. Liou, E.C. Nice, C. Huang, Y. Wei, Redox-sensitive cyclophilin A elicits chemoresistance through realigning cellular oxidative status in colorectal cancer, Cell Rep. 37 (2021) 110069.

[42] H.E. Greenwood, P.N. McCormick, T. Gendron, M. Glaser, R. Pereira, O.D.K. Maddocks, K. Sander, T. Zhang, N. Koglin, M.F. Lythgoe, E. Årstad, D. Hochhauser, T.H. Witney, Measurement of tumor antioxidant capacity and prediction of chemotherapy resistance in preclinical models of ovarian cancer by positron emission tomography, Clin. Cancer Res. : Off. J. Am. Assoc. Canc. Res. 25 (2019) 2471–2482.

[43] U.S. Srinivas, B.W.Q. Tan, B.A. Vellayappan, A.D. Jeyasekharan, ROS and the DNA damage response in cancer, Redox Biol. 25 (2019) 101084.

[44] J.N. Moloney, T.G. Cotter, ROS signalling in the biology of cancer, Semin. Cell Dev. Biol. 80 (2018) 50–64.

[45] R. Liu, J. Li, T. Zhang, L. Zou, Y. Chen, K. Wang, Y. Lei, K. Yuan, Y. Li, J. Lan, L. Cheng, N. Xie, R. Xiang, E.C. Nice, C. Huang, Y. Wei, Itraconazole suppresses the growth of glioblastoma through induction of autophagy: involvement of abnormal cholesterol trafficking, Autophagy 10 (2014) 1241–1255.

[46] Y. Zhang, J. Zhang, J. Gao, L. Wen, Pro-death or pro-survival: contrasting paradigms on nanomaterial-induced autophagy and exploitations for cancer therapy, Acc. Chem. Res. 52 (2019) 3164–3176.

[47] M.E. Lleonart, E. Abad, D. Graifer, A. Lyakhovich, Reactive oxygen species-mediated autophagy defines the fate of cancer stem cells, Antioxidants Redox Signal. 28 (2018) 1066–1079.

[48] S. Wei, T. Qiu, X. Yao, N. Wang, L. Jiang, X. Jia, Y. Tao, Z. Wang, P. Pei, J. Zhang, Y. Zhu, G. Yang, X. Liu, S. Liu, X. Sun, Arsenic induces pancreatic dysfunction and

ferroptosis via mitochondrial ROS-autophagy-lysosomal pathway, J. Hazard Mater. 384 (2020) 121390.

[49] G. Filomeni, D. De Zio, F. Cecconi, Oxidative stress and autophagy: the clash between damage and metabolic needs, Cell Death Differ. 22 (2015) 377–388.

[50] S. Mukhopadhyay, K.K. Mahapatra, P.P. Praharaj, S. Patil, S.K. Bhutia, Recent progress of autophagy signaling in tumor microenvironment and its targeting for possible cancer therapeutics, Semin. Cancer Biol. (2021).

[51] K. Ganesh, J. Massagué, Targeting metastatic cancer, Nat. Med. 27 (2021) 34–44.

[52] M. Liu, J. Yang, B. Xu, X. Zhang, Tumor metastasis: mechanistic insights and therapeutic interventions, MedComm 2 (2021) 587–617, 2020.

[53] Y. Liang, H. Zhang, X. Song, Q. Yang, Metastatic heterogeneity of breast cancer: molecular mechanism and potential therapeutic targets, Semin. Cancer Biol. 60 (2020) 14–27.

[54] C. Liang, L. Xu, G. Song, Z. Liu, Emerging nanomedicine approaches fighting tumor metastasis: animal models, metastasis-targeted drug delivery, phototherapy, and immunotherapy, Chem. Soc. Rev. 45 (2016) 6250–6269.

[55] J. Yu, Q. Mu, M. Fung, X. Xu, L. Zhu, R.J.Y. Ho, Challenges and opportunities in metastatic breast cancer treatments: nano-drug combinations delivered preferentially to metastatic cells may enhance therapeutic response, Pharmacol. Therapeut. (2022) 108108.

[56] Y. Ma, Y. Zhang, X. Li, Y. Zhao, M. Li, W. Jiang, X. Tang, J. Dou, L. Lu, F. Wang, Y. Wang, Near-infrared II phototherapy induces deep tissue immunogenic cell death and potentiates cancer immunotherapy, ACS Nano 13 (2019) 11967–11980.

[57] D.S. Oh, H.K. Lee, Autophagy protein ATG5 regulates CD36 expression and anti-tumor MHC class II antigen presentation in dendritic cells, Autophagy 15 (2019) 2091–2106.

[58] J. Richman, M. Dowsett, Beyond 5 years: enduring risk of recurrence in oestrogen receptor-positive breast cancer, Nat. Rev. Clin. Oncol. 16 (2019) 296–311.

[59] Y.K. Choi, B.K. Poudel, N. Marasini, K.Y. Yang, J.W. Kim, J.O. Kim, H.G. Choi, C.S. Yong, Enhanced solubility and oral bioavailability of itraconazole by combining membrane emulsification and spray drying technique, Int. J. Pharm. 434 (2012) 264–271.

[60] N.A. Vasilev, A.O. Surov, A.P. Voronin, K.V. Drozd, G.L. Perlovich, Novel cocrystals of itraconazole: insights from phase diagrams, formation thermodynamics and solubility, Int. J. Pharm. 599 (2021) 120441.

[61] H. Mei, S. Cai, D. Huang, H. Gao, J. Cao, B. He, Carrier-free nanodrugs with efficient drug delivery and release for cancer therapy: from intrinsic physicochemical properties to external modification, Bioact. Mater. 8 (2022) 220–240.

[62] Y. Qiao, Z. Wei, T. Qin, R. Song, Z. Yu, Q. Yuan, J. Du, Q. Zeng, L. Zong, S. Duan, Combined nanosuspensions from two natural active ingredients for cancer therapy with reduced side effects, Chin. Chem. Lett. 32 (2021) 2877–2881.

[63] S. Fu, G. Li, W. Zang, X. Zhou, K. Shi, Y. Zhai, Pure drug nano-assemblies: a facile carrier-free nanoplatform for efficient cancer therapy, Acta Pharm. Sin. B 12 (2022) 92–106.